ADVANCED MATERIALS
www.advmat.de

Ferrimagnetic Skyrmions in Topological Insulator/Ferrimagnet Heterostructures

Hao Wu, Felix Groß, Bingqian Dai, David Lujan, Seyed Armin Razavi, Peng Zhang, Yuxiang Liu, Kemal Sobotkiewich, Johannes Förster, Markus Weigand, Gisela Schütz, Xiaoqin Li, Joachim Gräfe, and Kang L. Wang**

Magnetic skyrmions are topologically nontrivial chiral spin textures that have potential applications in next-generation energy-efficient and high-density spintronic devices. In general, the chiral spins of skyrmions are stabilized by the noncollinear Dzyaloshinskii–Moriya interaction (DMI), originating from the inversion symmetry breaking combined with the strong spin–orbit coupling (SOC). Here, the strong SOC from topological insulators (TIs) is utilized to provide a large interfacial DMI in TI/ferrimagnet heterostructures at room temperature, resulting in small-size (radius ≈ 100 nm) skyrmions in the adjacent ferrimagnet. Antiferromagnetically coupled skyrmion sublattices are observed in the ferrimagnet by element-resolved scanning transmission X-ray microscopy, showing the potential of a vanishing skyrmion Hall effect and ultrafast skyrmion dynamics. The line-scan spin profile of the single skyrmion shows a Néel-type domain wall structure and a 120 nm size of the 180° domain wall. This work demonstrates the sizable DMI and small skyrmions in TI-based heterostructures with great promise for low-energy spintronic devices.

Magnetic skyrmions are topologically protected chiral spin textures, which can be treated as the quasi-particles in collinear magnetic systems.[1–4] The most significant difference between magnetic skyrmions and other magnetic structures such as magnetic bubbles is the nontrivial topology in real space, i.e., the nonzero topological charge n (winding number), which is obtained from the integral of the winding of the normalized local magnetization $n = \frac{1}{4\pi}\int \boldsymbol{m}\cdot\left(\frac{\partial \boldsymbol{m}}{\partial x}\times\frac{\partial \boldsymbol{m}}{\partial y}\right)\mathrm{d}x\,\mathrm{d}y$. Skyrmions are very sensitive to the spin torque, and the current density to move skyrmions is five to six orders of magnitude smaller than those to move magnetic domain walls.[5] Due to the small size, low-power dissipation, and robustness to external perturbations, magnetic skyrmion-based devices are considered as a promising candidate for the next-generation memory and logic technology.

Generally, magnetic skyrmions are stabilized by the noncollinear Dzyaloshinskii–Moriya interaction (DMI),[6,7] and the Hamiltonian describing DMI can be written as $\hat{H}_{\mathrm{DMI}} = \sum_{i,j} -\mathbf{D}_{ij}\cdot(\boldsymbol{m}_i \times \boldsymbol{m}_j)$, where $\mathbf{D}_{ij}$ is the DMI tensor between magnetic moments $\boldsymbol{m}_i$ and $\boldsymbol{m}_j$. In a microscopic picture, DMI originates from the strong spin–orbit coupling (SOC) combined with the inversion symmetry breaking, such as the crystal symmetry breaking in bulk crystals and the structural symmetry breaking at the interface of magnetic multilayers.[8–10] Topological insulators (TIs) with insulating bulk and conducting surface possess a strong SOC,[11] which is manifested by the spin-momentum locking of the topological surface states,[12] therefore, in principle, there should be a large DMI and the induced skyrmions in the topological interface.[13–15] Recently, several works reported the topological Hall effect (THE) in TI-based heterostructures,[16–19] giving the indirect evidence of skyrmions. However, direct observation of DMI and skyrmions in TI-based heterostructures still remains to be discovered. Such observations are critical since they would rule out other trivial explanations of THE such as nonlinear anomalous Hall effect.[20] Furthermore, spin-momentum locked surface states in TIs contribute to a giant spin–orbit torque (SOT) even at room temperature.[21–25] Thus, TI-based heterostructures that combine small skyrmions and giant SOT can provide a promising route for the high-density and ultralow power spintronic devices.

In this work, we demonstrate sizable DMI and small skyrmions in TI/ferrimagnet heterostructures at room temperature. The large DMI coefficient is measured by the Brillouin light scattering (BLS) method in this system, which is comparable with heavy metals with strong SOC. Small skyrmions with a

Dr. H. Wu, B. Q. Dai, S. A. Razavi, P. Zhang, Y. X. Liu, Prof. K. L. Wang
Department of Electrical and Computer Engineering
and Department of Physics and Astronomy
University of California
Los Angeles, CA 90095, USA
E-mail: wang@ee.ucla.edu

F. Groß, Dr. J. Förster, Dr. M. Weigand, Dr. G. Schütz, Dr. J. Gräfe
Max Planck Institute for Intelligent Systems
Heisenbergstraße 3, Stuttgart 70569, Germany
E-mail: graefe@is.mpg.de

D. Lujan, K. Sobotkiewich, Prof. X. Q. Li
Department of Physics
and Center for Complex Quantum Systems
The University of Texas at Austin
Austin, TX 78712, USA

The ORCID identification number(s) for the author(s) of this article can be found under https://doi.org/10.1002/adma.202003380.

DOI: 10.1002/adma.202003380

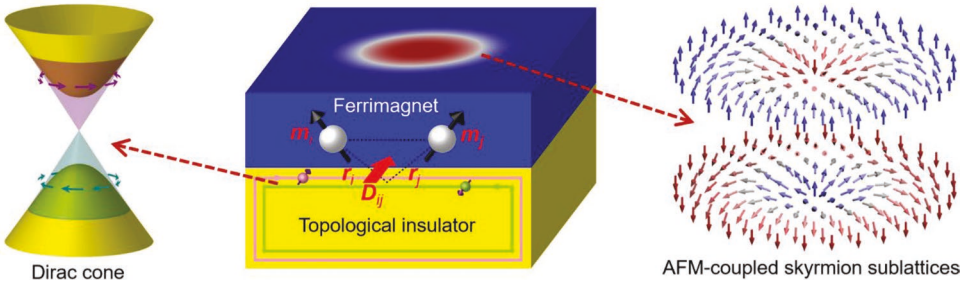

Figure 1. Schematic of DMI and skyrmions in TI/ferrimagnet heterostructures. In topological insulator (TI)/ferrimagnet heterostructures, the strong spin–orbit coupling (SOC) in TIs combined with the structural inversion symmetry breaking by the interface produces the interfacial Dzyaloshinskii–Moriya interaction (DMI), which stabilizes the magnetic skyrmions in the ferrimagnet. The unique Dirac cone band structure of topological surface states gives rise to the spin-momentum locking, indicating the strong SOC in TIs. The antiferromagnetically coupled (AFM-coupled) skyrmion sublattices in the ferrimagnet.

radius around 100 nm are measured by scanning transmission X-ray microscopy (STXM), and the Néel-type domain wall structure is verified by the line-scan spin profile of the single skyrmion. Antiferromagnetically coupled (AFM-coupled) skyrmion sublattices from Gd and Fe elements are observed by the element-resolved STXM, showing the potential of vanishing skyrmion Hall effect and ultrafast skyrmion dynamics.[26–29] This work opens a promising route to utilize the topological insulators for energy-efficient and high-density skyrmion devices.

Figure 1 shows the schematic of DMI and skyrmions in the $(BiSb)_2Te_3$ (6 nm)/GdFeCo (t nm) heterostructure, where the topological insulator $(BiSb)_2Te_3$ and the ferrimagnet GdFeCo are grown by molecular beam epitaxy and magnetron sputtering methods, respectively. Spin-momentum locking of Dirac cone band structure in $(BiSb)_2Te_3$ gives rise to the spin polarized electron transport in the topological surface states, where utilizing the giant SOT from topological surface states to manipulate the magnetic moment has been realized at room temperature,[21–25] indicating the strong SOC in TIs.

At the same time, the strong SOC in topological insulators combined with the structural inversion symmetry breaking by the interface of the heterostructure induces the noncollinear interfacial DMI, i.e., $\mathbf{D}_{ij} = D(\mathbf{r}_i \times \mathbf{r}_j)$, where D is the interfacial DMI coefficient. Interfacial DMI provides a superexchange interaction between neighboring magnetic moments $\boldsymbol{m}_i$ and $\boldsymbol{m}_j$ in the adjacent ferrimagnet (GdFeCo) by the medium of the strong SOC in TIs, which stabilizes the magnetic skyrmions. Both DMI and perpendicular magnetic anisotropy (PMA) are essential for the skyrmion formation. However, there is a competition between PMA and DMI:PMA aligns the magnetic moments along the easy axis, while DMI cants the neighboring magnetic moments.[30] We carefully adjust the PMA via the composition and thickness of GdFeCo and find that magnetic skyrmions are formed in a 8 nm GdFeCo with the 26% concentration of Gd. GdFeCo is a ferrimagnet with two AFM-coupled spin sublattices (Gd and FeCo),[31] as a result, the AFM-coupled skyrmion sublattices are formed in this system accordingly, as shown in Figure 1.

To evaluate the interfacial DMI, momentum-resolved Brillouin light scattering (BLS) spectrum is performed to map the interfacial DMI-induced asymmetric spin wave dispersion in $(BiSb)_2Te_3$/GdFeCo. **Figure 2**a shows the schematic of the BLS measurement set up, where a constant magnetic field $B = 0.21$ T along the $-y$ direction is applied during the measurements. An s-polarized laser beam is incident onto the magnetic film with an angle θ and the p-polarized component of the backscattered light is detected. For the inelastic light scattering process in magnetic thin films, only the in-plane wavevector $\left(k_x = \frac{2\pi}{\lambda}\sin\theta\right)$ is conserved, where λ is the laser wavelength (532 nm). The Stokes and anti-Stokes peaks of BLS spectra correspond to the creation and annihilation of magnons, with $k_M = \Delta k_x = 2k_x = \frac{4\pi}{\lambda}\sin\theta$ along the $-x$ and $+x$ directions, respectively.

At the $(BiSb)_2Te_3$/GdFeCo interface, the spatial chirality of the surface spin wave depends on the propagation direction with respect to the direction of the magnetization. In the presence of the interfacial DMI, one spatial chirality is energetically preferred according to the sign of D (right-hand for positive D), resulting in the asymmetric spin wave dispersion,[32,33] as shown in Figure 2b. Figure 2c shows the Stokes ($-k_M$) and anti-Stokes (k_M) peaks of BLS measured in $(BiSb)_2Te_3$/GdFeCo, where the frequency shift $2\Delta f_{DMI}$ between the Stokes and anti-Stokes frequencies indicates the existence of the interfacial DMI. Figure 2d shows the Δf_{DMI} as a function of k_x, by fitting the Δf_{DMI}–k_x curve with $\Delta f_{DMI} = \frac{2\gamma}{\pi M_s} D k_x$, the DMI coefficient $D = 35.5 \pm 0.25$ μJ m^{-2} is obtained for $(BiSb)_2Te_3$/GdFeCo, which is comparable with that in the Ta/CoFeB interface (36.0 μJ m^{-2}),[34] where γ is the gyromagnetic ratio (2.0) and M_s is the saturation magnetization (6.7×10^4 A m^{-1}). Without $(BiSb)_2Te_3$, the DMI coefficient in a single GdFeCo film is significantly reduced, as shown in Figure 2d, indicating the role of the strong SOC from the topological insulators.

Scanning transmission X-ray microscopy (STXM)[35,36] is performed to image the magnetic domain structures in $(BiSb)_2Te_3$/GdFeCo. We first saturate the magnetic domains to the $-z$ direction with a negative out-of-plane magnetic field. Then the magnetic field is reduced to 0 mT to obtain the remanent magnetization state, where the strip domains with the central magnetization along the $-z$ direction ($-M_z$) form, as shown in **Figure 3**. The color transition from red to blue represents the z-component magnetization transition from $-M_z$ to $+M_z$.

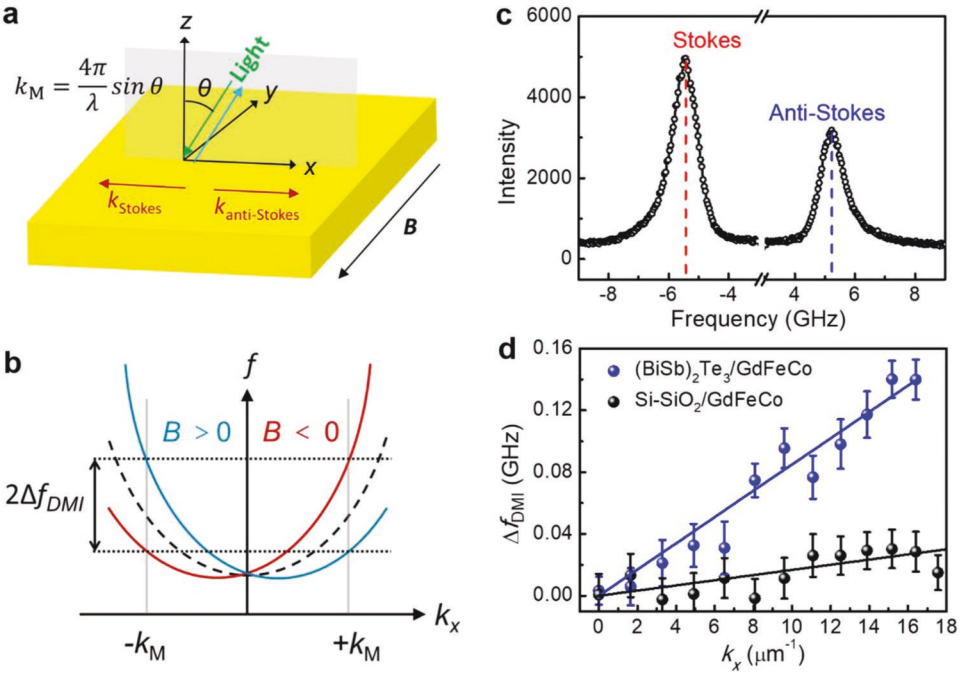

Figure 2. BLS measurement to quantify DMI. a) Schematic of the Brillouin light scattering (BLS) spectrum measurement. Under a magnetic field along the $-y$ direction, a laser beam which is incident to the film plane with an angle of θ, creates (annihilates) magnons along the $-x$ ($+x$) direction. b) DMI-induced asymmetric spin wave dispersion with the magnetic field of $\pm B$ (solid line), respectively, where the dashed line shows the symmetric spin wave dispersion without the magnetic field. c) BLS spectra of Stokes and anti-Stokes peaks, where the applied magnetic field is 0.21 T. d) DMI-induced spin wave frequency shift Δf_{DMI} as a function of wave vector k_x measured from $(BiSb)_2Te_3$/GaFeCo (blue) and from a control sample Si–SiO_2/GdFeCo (black), and the dashed line shows the linear fitting curve.

When we increase the out-of-plane magnetic field B from 0 to +8 mT, the strip domains with $-M_z$ continue to shrink, until the inside domains vanish and the domain walls merge together, forming the skyrmion states. These skyrmions can be moved by the current-induced SOT (Section S3, Supporting Information), indicating that the skyrmions in this system come from the interfacial DMI, rather than the pinning centers at the interface.[37]

The magnetic field dependence of the skyrmion bubble radius is shown in **Figure 4**, where the size of the circles represents the proportion of skyrmion bubbles of each radius at one specific field, and the blue dashed line represents the average radius of skyrmion bubbles at each field. With increasing the magnetic field from 0 to +4 mT, the average size of skyrmion bubbles is significantly reduced, because the positive magnetic field ($+z$) shrinks the inside magnetic domains of skyrmion bubbles with $-M_z$. While the size of skyrmion bubbles does not change too much above +4 mT, indicating that most inside magnetic domains have vanished and the pure skyrmion states are formed. In addition, the distribution of the size of skyrmion bubbles is much concentrated at the larger magnetic field, which also indicates the Zeeman energy-induced phase transition from trivial magnetic bubbles to skyrmions.

GdFeCo is a ferrimagnetic material with two AFM-coupled spin sublattices, i.e., Gd and FeCo sublattices, therefore, the element-resolved STXM measurement[38] has the capability to obtain the individual spin textures from these AFM-coupled sublattices. By tuning the X-ray energy from the Gd M_5 (1186.4 eV) to the Fe L_3 (708.8 eV) absorption edges, the sensitivity of the absorption signal is changed from the Gd to the Fe sublattices. The incident X-ray is circular polarized to right-hand and left-hand (σ^+ and σ^-) for the imaging, respectively, and the pure spin-resolved textures are obtained by dividing these two contributions (σ^+ and σ^-), as shown in **Figure 5**a.

Figure 5b shows the STXM mapping for the Gd and Fe spin sublattices, respectively, where the size of arrows represents the amplitude of the out-of-plane (z) component of magnetization (M_z), and the color transition from red to blue represents the z-component magnetization transition from $-M_z$ to $+M_z$. From Figure 5b, we can clearly see that the skyrmion sublattices from the Gd and Fe elements are AFM-coupled, and the two 3D rendered pictures actually display the AFM-coupled skyrmion sublattices at the same position: one in the Gd lattice and one in the Fe lattice, indicating the strong exchange interaction between Gd and CoFe spin sublattices. The ferrimagnetic skyrmions can potentially reduce the skyrmion Hall effect that shifts the skyrmions toward the edges of skyrmion-based devices, supporting a long skyrmion propagation length.[26–28] At the same time, more than 100 GHz magnetic resonance frequency in the ferrimagnet promises the ultrafast spin dynamics of ferrimagnetic skyrmions.[39]

Next, we focus on the detailed spin profile of a single skyrmion. The sample is raster-scanned while the focused X-ray beam remains fixed, and the transmission intensity of X-ray is detected for every position, where the X-ray beam is tilted an angle of 30° from z-direction in the x-z plane to be sensitive to the $-x$ and $+z$ components of magnetization, as shown in

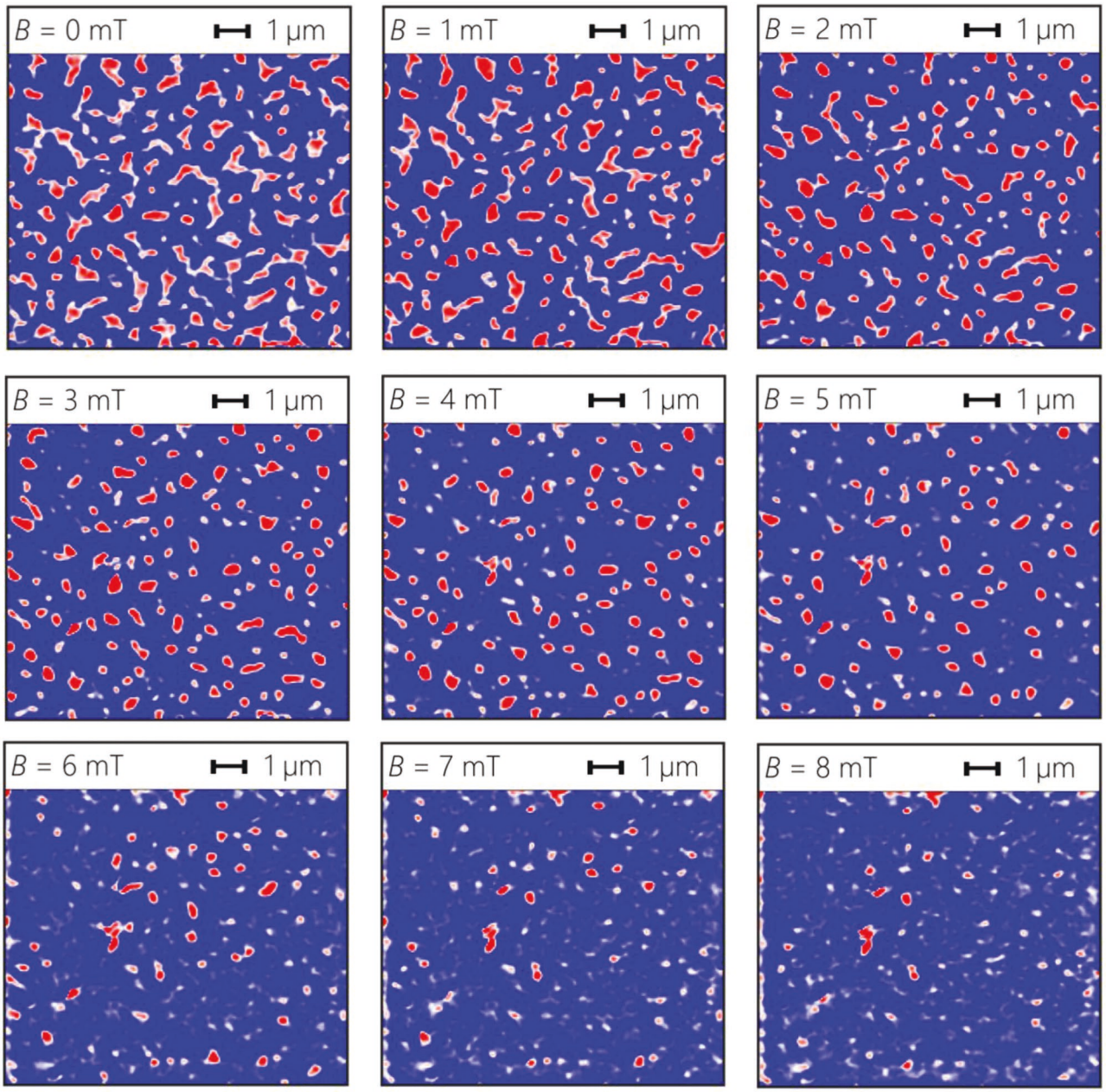

Figure 3. Magnetic field dependences of skyrmions. With a negative out-of-plane magnetic field (–*z*) to saturate the magnetization to $-M_z$ direction first, and then the magnetic field ranging from 0 to +8 mT is applied to transform the stripe domains to magnetic skyrmions by shrink the $-M_z$ inside magnetic domains. The color transition from red to blue represents the *z*-component magnetization transition from $-M_z$ to $+M_z$.

Figure 6a,d. The total line-scan contrast is the summation of the *z* (63.4%) and *x* (36.6%) components of magnetization. With the X-ray beam scanning along the *x* direction, the spin profile shows a continuous 360° spin-spiral transition over the range of the double domain wall size, as shown in Figure 6b, where the asymmetric line-scan curve indicates the Néel-type domain wall structure (↑→↓←↑).[40] The reason is as follows: for the *z*-component magnetization m_z, the line-scan curve should be symmetric; while for the *x*-component magnetization m_x of Néel-type domains, the antiparallel and parallel orientations between m_x and the in-plane sensitive direction (–*x*) of X-ray contribute to the negative and positive signals, respectively, and thus resulting in the asymmetric line-scan curve. The dip between up–down magnetizations and the peak between down–up magnetizations in Figure 6b demonstrate the antiparallel and parallel orientations with the in-plane sensitive direction (–*x*) of the X-rays, respectively, indicating a right-hand chirality of skyrmions (↑→↓←↑), which is consistent with the positive sign of the DMI coefficient in this system. Meanwhile, for the line-scan contrast along the *y* direction, the symmetric curve shows zero *x*-component of the magnetization, as shown in Figure 6c, supporting the Néel-type domain wall structure.

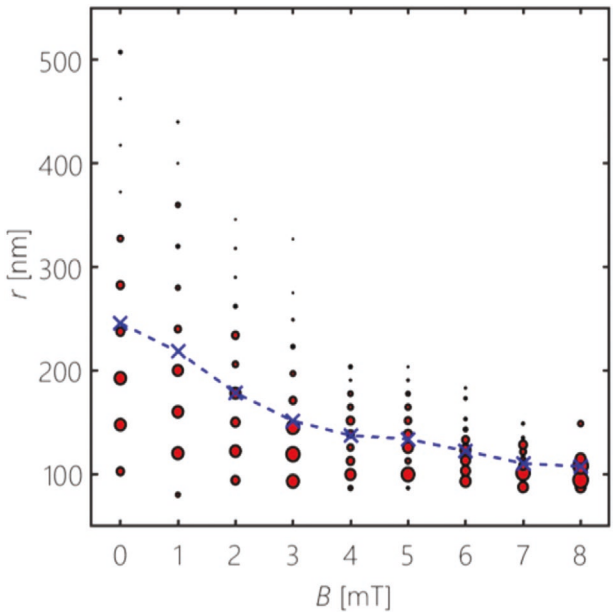

Figure 4. The size of the skyrmion bubbles as a function of the magnetic field. The out-of-plane magnetic field dependence of the radius of skyrmion bubbles, where the size of the circles represents the proportion of skyrmion bubbles of each radius at one specific field, and the blue dashed line represents the average radius of skyrmion bubbles at each field.

The line-scan spin profile of the singe skyrmion in Figure 6b can be fitted with $\tan\frac{\Theta_0}{2}=\frac{r_{sk}}{r}e^{\xi(r_{sk}-r)}$, where Θ_0 is the polar angle, r_{sk} is the reduced equilibrium radius of skyrmions defined as $M_z(r) = 0$, $\xi = 2K_u/\mu_0 M_s^2 - 1$, and K_u is the perpendicular magnetic anisotropy energy.[41] From the fitting, we can get the r_{sk} of 60 nm. From the field dependence of the skyrmion size in Figure 4, the minimum average radius of skyrmion is around 107 nm, which is close to the 180° domain wall size of $2r_{sk}$ = 120 nm obtained from the line-scan spin profile fitting of the singe skyrmion.

In summary, we explicitly measured the interfacial DMI and demonstrated the ferrimagnetic skyrmions in topological insulator/ferrimagnet heterostructures. A large interfacial DMI obtained from the BLS measurement comes from the strong SOC in topological insulators combined with the structural inversion symmetry breaking by the interface. Small-size skyrmions (radius around 100 nm) are observed by the STXM at room temperature, which are stabilized by the interfacial DMI from the topological interface. AFM-coupled skyrmion sublattices from Gd and Fe elements are distinguished by the element-resolved STXM measurement, which show the potential of vanishing skyrmion Hall effect and ultrafast skyrmion dynamics. The line-scan spin profile of the single skyrmion indicates the Néel-type domain wall structure and a 120 nm size of the 180° domain wall. This work will inspire the investigation of the real-space topological spin textures in TI-based heterostructures, where combining small skyrmions and giant SOT provides a promising route for the next-generation spintronic devices.

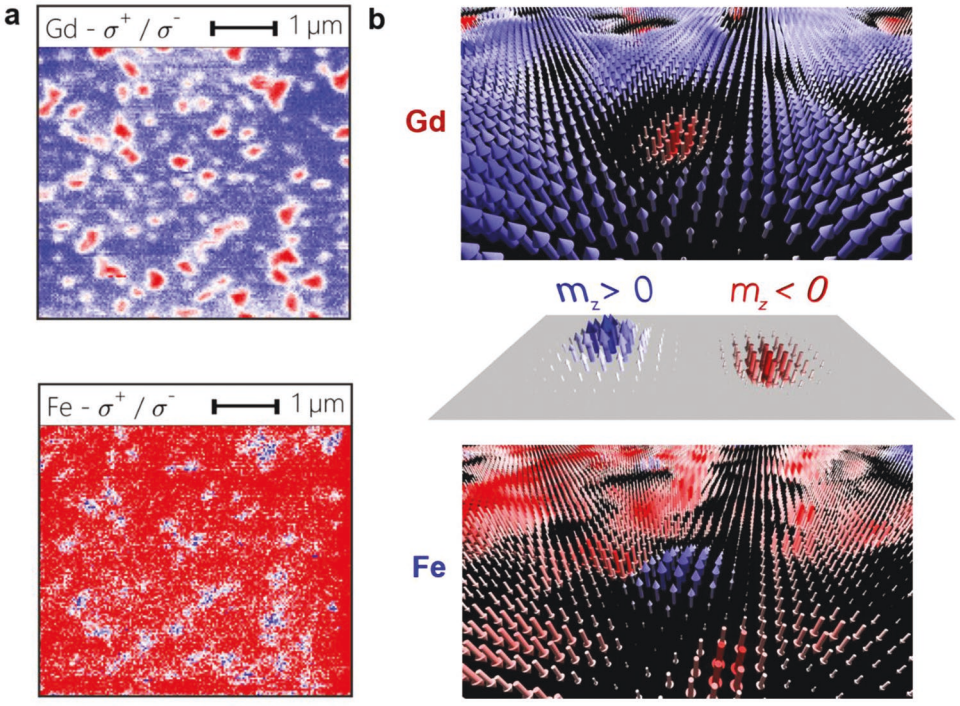

Figure 5. Ferrimagnetic skyrmions. a) The 2D AFM-coupled skyrmion sublattices from Gd and Fe elements, which are measured by the element-resolved STXM. The STXM is measured with the right-hand (σ^+) and left-hand (σ^-) circular polarizations, respectively, where dividing these two contributions leads to the pure spin-resolved texture. b) The 3D AFM-coupled skyrmion sublattices from Gd and Fe elements, where the size of arrows represents the magnitude of M_z components, and the color transition from red to blue represents the *z*-component magnetization transition from $-M_z$ to $+M_z$.

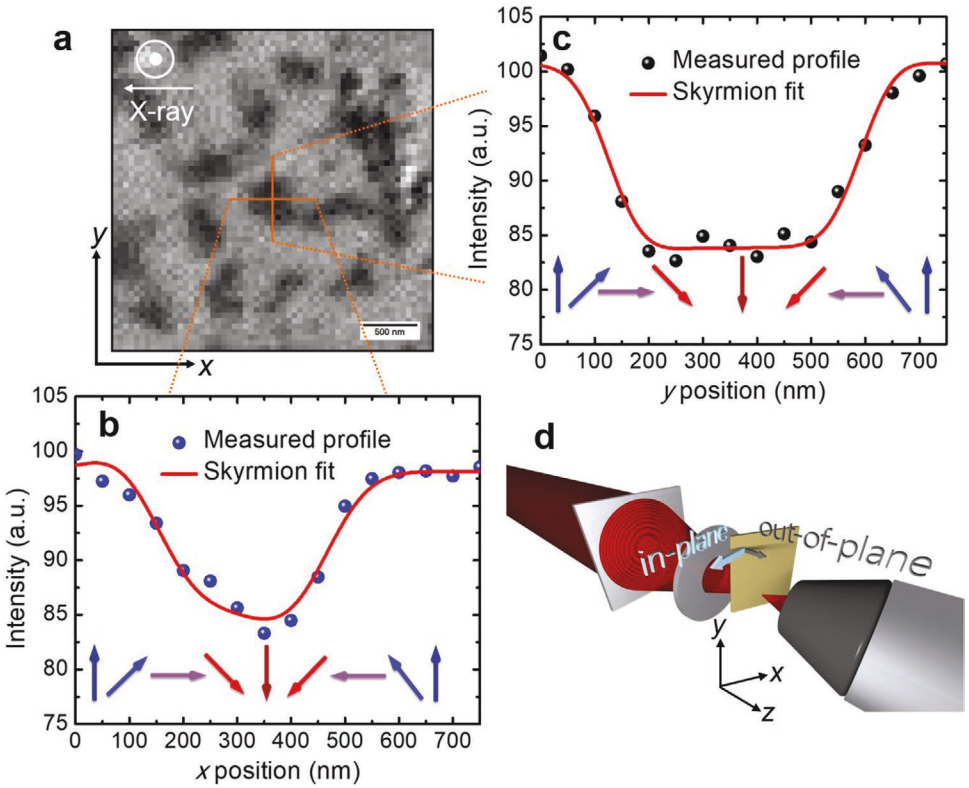

Figure 6. Line-scan spin profile of a single skyrmion. a) Schematic of two scanning lines of X-ray beam along the *x* and *y* directions for the single skyrmion, where the X-ray beam is tilted an angle to be sensitive to the $-x$ and $+z$ components of magnetization. b) Transmission X-ray intensity as a function of *x* positions shows a continuous 360° spin spiral transition of the single skyrmion, where the asymmetric curve indicates the Néel-type domain wall structure (↑→↓←↑). c) Spin–spiral transition of the single skyrmion along the *y* direction, where the symmetric curve shows the zero *x*-component of magnetization, supporting the Néel-type domain wall structure. d) Sketch of the line-scan spin profile measurement. The sample is raster-scanned while the focused the X-ray beam remains fixed, and the transmission intensity of X-ray is detected for every position. The X-ray beam is tilted an angle of 30° from *z*-direction in the *x*–*z* plane.

Experimental Section

Sample Growth: The topological insulators of $(BiSb)_2Te_3$ were grown on $Al_2O_3(0001)$ substrates by the molecular beam epitaxy (MBE) method. A 600 °C preannealing was performed to clean the surface of substrates, and the substrate temperature was 200 °C during the growth. The layer-by-layer epitaxial growth was monitored by the reflection high-energy electron diffraction (RHEED). The $Gd_x(FeCo)_{1-x}$ films were deposited by the magnetron sputtering method with cosputtering of Gd and FeCo targets, where the substrates kept rotating during the deposition. A 10 nm Te capping layer was used to protect the $(BiSb)_2Te_3$ surface during the sample transfer from MBE to sputtering chambers through air, and then removed by a 220 °C annealing. The composition of $Gd_x(FeCo)_{1-x}$ was tuned by the power of Gd and FeCo targets, and the Ar pressure for deposition was 3 mTorr. A 2 nm Al_2O_3 capping layer was deposited on the top to avoid the films to be oxidized.

Magnetic Properties Measurement: The magnetic properties were measured by a magneto-optic Kerr effect (MOKE) system, vibrating sample magnetometer (VSM), and superconducting quantum interference device (SQUID, Quantum Design) magnetometer. The magnetic domains and DMI-induced asymmetric magnetic domain nucleation at edges were measured by a MOKE imaging system.

Scanning Transmission X-Ray Microscopy (STXM) Measurement: STXM measurements were conducted at the MPI IS operated MAXYMUS end station at the UE46-PGM2 beam line at the BESSY II synchrotron radiation facility. Samples were illuminated using a zone plate with a resolution below 18 nm under normal and 30° grazing incidence for magnetic sensitivity in the out-of-plane and in-plane directions, respectively. Therefore, for the normal-incidence direction, the X-rays were only sensitive to the *z* magnetization; for the 30° incidence angle, the *z* magnetization contributes $\cos(30°)/[\cos(30°) + \sin(30°)] \approx 63.4\%$ to the total X-ray intensity, while the *x* magnetization contributes $\sin(30°)/[\cos(30°) + \sin(30°)] \approx 36.6\%$. The photon energies were set to 708.8 and 1186.4 eV to get maximum XMCD contrast at the Fe L_3 and Gd M_5 absorption edges, respectively. The surface-sensitive total electron yield (TEY) signal was detected as the sample drain current that was amplified by a FEMTO DLPCA-200 low noise amplifier. During the measurements an out-of-plane field of up to 240 mT was applied that was generated by a set of four rotatable permanent magnets.

Supporting Information

Supporting Information is available from the Wiley Online Library or from the author.

Acknowledgements

The authors thank HZB (Berlin, Germany) for the allocation of synchrotron radiation beamtime. This work was supported by the NSF Award Nos. 1611570 and 1810163, the Nanosystems Engineering Research Center for Translational Applications of Nanoscale Multiferroic Systems (TANMS), the U.S. Army Research Office MURI program under

Grants No. W911NF-16-1-0472 and No. W911NF-15-1-10561, and the Spins and Heat in Nanoscale Electronic Systems (SHINES) Center funded by the US Department of Energy (DOE), under Award No. DE-SC0012670. D.L. and X.L. are funded by an NSF MRSEC under Cooperative Agreement No. DMR-1720595. H.W. acknowledges helpful discussions with Prof. Ying Zhang from IOP, CAS. Open access funding enabled and organized by Projekt DEAL.

Conflict of Interest

The authors declare no conflict of interest.

Keywords

Dzyaloshinskii–Moriya interaction, ferrimagnetic skyrmions, ferrimagnets, topological insulators

Received: May 17, 2020
Published online: July 14, 2020

[1] A. Fert, N. Reyren, V. Cros, *Nat. Rev. Mater.* **2017**, *2*, 17031.
[2] N. Nagaosa, Y. Tokura, *Nat. Nanotechnol.* **2013**, *8*, 899.
[3] N. Romming, C. Hanneken, M. Menzel, J. E. Bickel, B. Wolter, K. von Bergmann, A. Kubetzka, R. Wiesendanger, *Science* **2013**, *341*, 636.
[4] W. Jiang, P. Upadhyaya, W. Zhang, G. Yu, M. B. Jungfleisch, F. Y. Fradin, J. E. Pearson, Y. Tserkovnyak, K. L. Wang, O. Heinonen, S. G. E. te Velthuis, A. Hoffmann, *Science* **2015**, *349*, 283.
[5] A. Fert, V. Cros, J. Sampaio, *Nat. Nanotechnol.* **2013**, *8*, 152.
[6] I. Dzyaloshinsky, *J. Phys. Chem. Solids* **1958**, *4*, 241.
[7] T. Moriya, *Phys. Rev.* **1960**, *120*, 91.
[8] A. Fert, P. M. Levy, *Phys. Rev. Lett.* **1980**, *44*, 1538.
[9] P. M. Levy, A. Fert, *Phys. Rev. B* **1981**, *23*, 4667.
[10] H. Yang, A. Thiaville, S. Rohart, A. Fert, M. Chshiev, *Phys. Rev. Lett.* **2015**, *115*, 267210.
[11] J. E. Moore, *Nature* **2010**, *464*, 194.
[12] D. Hsieh, Y. Xia, D. Qian, L. Wray, J. H. Dil, F. Meier, J. Osterwalder, L. Patthey, J. G. Checkelsky, N. P. Ong, A. V. Fedorov, H. Lin, A. Bansil, D. Grauer, Y. S. Hor, R. J. Cava, M. Z. Hasan, *Nature* **2009**, *460*, 1101.
[13] S. Zhang, F. Kronast, G. van der Laan, T. Hesjedal, *Nano Lett.* **2018**, *18*, 1057.
[14] H. M. Hurst, D. K. Efimkin, J. Zang, V. Galitski, *Phys. Rev. B* **2015**, *91*, 060401(R).
[15] F. S. Nogueira, I. Eremin, F. Katmis, J. S. Moodera, J. van den Brink, V. P. Kravchuk, *Phys. Rev. B* **2018**, *98*, 060401(R).
[16] K. Yasuda, R. Wakatsuki, T. Morimoto, R. Yoshimi, A. Tsukazaki, K. S. Takahashi, M. Ezawa, M. Kawasaki, N. Nagaosa, Y. Tokura, *Nat. Phys.* **2016**, *12*, 555.
[17] C. Liu, Y. Zang, W. Ruan, Y. Gong, K. He, X. Ma, Q.-K. Xue, Y. Wang, *Phys. Rev. Lett.* **2017**, *119*, 176809.
[18] Q. L. He, G. Yin, A. J. Grutter, L. Pan, X. Che, G. Yu, D. A. Gilbert, S. M. Disseler, Y. Liu, P. Shafer, B. Zhang, Y. Wu, B. J. Kirby, E. Arenholz, R. K. Lake, X. Han, K. L. Wang, *Nat. Commun.* **2018**, *9*, 2767.
[19] J. Chen, L. Wang, M. Zhang, L. Zhou, R. Zhang, L. Jin, X. Wang, H. Qin, Y. Qiu, J. Mei, F. Ye, B. Xi, H. He, B. Li, G. Wang, *Nano Lett.* **2019**, *19*, 6144.
[20] V. K. Dugaev, M. Inglot, E. Y. Sherman, J. Berakdar, J. Barnaś, *Phys. Rev. Lett.* **2012**, *109*, 206601.
[21] J. Han, A. Richardella, S. A. Siddiqui, J. Finley, N. Samarth, L. Liu, *Phys. Rev. Lett.* **2017**, *119*, 077702.
[22] M. Dc, R. Grassi, J.-Y. Chen, M. Jamali, D. Reifsnyder Hickey, D. Zhang, Z. Zhao, H. Li, P. Quarterman, Y. Lv, M. Li, A. Manchon, K. A. Mkhoyan, T. Low, J.-P. Wang, *Nat. Mater.* **2018**, *17*, 800.
[23] N. H. D. Khang, Y. Ueda, P. N. Hai, *Nat. Mater.* **2018**, *17*, 808.
[24] Y. Wang, D. Zhu, Y. Wu, Y. Yang, J. Yu, R. Ramaswamy, R. Mishra, S. Shi, M. Elyasi, K.-L. Teo, Y. Wu, H. Yang, *Nat. Commun.* **2017**, *8*, 1364.
[25] H. Wu, Y. Xu, P. Deng, Q. Pan, S. A. Razavi, K. Wong, L. Huang, B. Dai, Q. Shao, G. Yu, X. Han, J.-C. Rojas-Sánchez, S. Mangin, K. L. Wang, *Adv. Mater.* **2019**, *31*, 1901681.
[26] S. Woo, K. Song, X. Zhang, Y. Zhou, M. Ezawa, X. Liu, S. Finizio, J. Raabe, N. Lee, S. Kim, S. Park, Y. Kim, J. Kim, D. Lee1, O. Lee, J. Choi, B. Min, H. Koo, J. Chang, *Nat. Commun.* **2018**, *9*, 959.
[27] Y. Hirata, D.-H. Kim, S. K. Kim, D.-K. Lee, S.-H. Oh, D.-Y. Kim, T. Nishimura, T. Okuno, Y. Futakawa, H. Yoshikawa, A. Tsukamoto, Y. Tserkovnyak, Y. Shiota, T. Moriyama, S.-B. Choe, K.-J. Lee, T. Ono, *Nat. Nanotechnol.* **2019**, *14*, 232.
[28] W. Jiang, X. Zhang, G. Yu, W. Zhang, X. Wang, M. B. Jungfleisch, J. E. Pearson, X. Cheng, O. Heinonen, K. L. Wang, Y. Zhou, A. Hoffmann, S. G. E. te Velthuis, *Nat. Phys.* **2017**, *13*, 162.
[29] L. Caretta, M. Mann, F. Büttner, K. Ueda, B. Pfau, C. M. Günther, P. Hessing, A. Churikova, C. Klose, M. Schneider, D. Engel, C. Marcus, D. Bono, K. Bagschik, S. Eisebitt, G. S. D. Beach, *Nat. Nanotechnol.* **2018**, *13*, 1154.
[30] G. Yu, P. Upadhyaya, X. Li, W. Li, S. K. Kim, Y. Fan, K. L. Wong, Y. Tserkovnyak, P. K. Amiri, K. L. Wang, *Nano Lett.* **2016**, *16*, 1981.
[31] I. Radu, K. Vahaplar, C. Stamm, T. Kachel, N. Pontius, H. A. Dürr, T. A. Ostler, J. Barker, R. F. L. Evans, R. W. Chantrell, A. Tsukamoto, A. Itoh, A. Kirilyuk, T. Rasing, A. V. Kimel, *Nature* **2011**, *472*, 205.
[32] H. T. Nembach, J. M. Shaw, M. Weiler, E. Jué, T. J. Silva, *Nat. Phys.* **2015**, *11*, 825.
[33] J. Cho, N.-H. Kim, S. Lee, J.-S. Kim, R. Lavrijsen, A. Solignac, Y. Yin, D.-S. Han, N. J. J. van Hoof, H. J. M. Swagten, B. Koopmans, C.-Y. You, *Nat. Commun.* **2015**, *6*, 7635.
[34] X. Ma, G. Yu, C. Tang, X. Li, C. He, J. Shi, K. L. Wang, X. Li, *Phys. Rev. Lett.* **2018**, *120*, 157204.
[35] I. Bykova, K. Keskinbora, U. Sanli, J. Gräfe, M. Bechtel, G. Yu, E. Goering, H. Stoll, G. Schütz, M. Weigand, *Microsc. Microanal.* **2018**, *24*, 34.
[36] P. Fischer, *IEEE Trans. Magn.* **2015**, *51*, 0800131.
[37] G. Yu, P. Upadhyaya, Q. Shao, H. Wu, G. Yin, X. Li, C. He, W. Jiang, X. Han, P. K. Amiri, K. L. Wang, *Nano Lett.* **2017**, *17*, 261.
[38] V. Ukleev, Y. Yamasaki, D. Morikawa, K. Karube, K. Shibata, Y. Tokunaga, Y. Okamura, K. Amemiya, M. Valvidares, H. Nakao, Y. Taguchi, Y. Tokura, T. Arima, *Phys. Rev. B* **2019**, *99*, 144408.
[39] C. D. Stanciu, A. V. Kimel, F. Hansteen, A. Tsukamoto, A. Itoh, A. Kirilyuk, T. Rasing, *Phys. Rev. B* **2006**, *73*, 220402.
[40] O. Boulle, J. Vogel, H. Yang, S. Pizzini, D. de Souza Chaves, A. Locatelli, T. O. Menteş, A. Sala, L. D. Buda-Prejbeanu, O. Klein, M. Belmeguenai, Y. Roussigné, A. Stashkevich, S. M. Chérif, L. Aballe, M. Foerster, M. Chshiev, S. Auffret, I. M. Miron, G. Gaudin, *Nat. Nanotechnol.* **2016**, *11*, 449.
[41] N. Romming, A. Kubetzka, C. Hanneken, K. von Bergmann, R. Wiesendanger, *Phys. Rev. Lett.* **2015**, *114*, 177203.